Available online at www.sciencedirect.com
SCIENCE DIRECT®
Polymer 45 (2004) 2931–2939
polymer
www.elsevier.com/locate/polymer

Comparison of crystallization kinetics in various nanoconfined geometries

Lu Sun[a], Lei Zhu[a,*], Qing Ge[b], Roderic P. Quirk[b], Chenchen Xue[b], Stephen Z.D. Cheng[b], Benjamin S. Hsiao[c], Carlos A. Avila-Orta[c], Igors Sics[c], Marie E. Cantino[d]

[a]*Polymer Program, Institute of Materials Science and Department of Chemical Engineering, The University of Connecticut, Storrs, CT 06269-3136, USA*
[b]*Maurice Morton Institute and Department of Polymer Science, The University of Akron, Akron, OH 44325, USA*
[c]*Department of Chemistry, State University of New York at Stony Brook, Stony Brook, NY 11794, USA*
[d]*Department of Physiology and Neurobiology, The University of Connecticut, Storrs, CT 06269, USA*

Received 7 December 2003; received in revised form 13 February 2004; accepted 14 February 2004

Abstract

Phase morphological effect on crystallization kinetics in various nanoconfined spaces in a polystyrene-*block*-poly(ethylene oxide) (PS-*b*-PEO) diblock copolymer with a PEO volume fraction of 37 vol% was investigated. The phase morphology was characterized by small-angle X-ray scattering and transmission electron microscopy techniques. When the sample was cast from chloroform solution and annealed at 150 °C, a double gyroid (DG) phase was obtained. After it was subjected to a large-amplitude reciprocating shear, the sample transformed to an oriented hexagonal cylinder (Hex) phase. To obtain a lamellar confined geometry, lamellar single crystals were grown from dilute solutions. The crystallization in the lamellar (Lam) phase was one-dimensionally (1D) confined, while it was two-dimensionally (2D) confined in the DG and Hex phases, although they had different structures. Differential scanning calorimetry (DSC) was employed to study the crystallization kinetics using the Avrami analysis for these three nanoconfined geometries. Heterogeneous nucleation was found in all three samples in the crystallization temperature (T_c) regions studied. DSC results indicated that the crystallization kinetics in the Lam phase was the fastest, and the PEO crystals possessed higher thermodynamic stability than in the DG and Hex phases. For the crystallization kinetics in two 2D-confined phases, at low T_c (<35 °C) the PEO crystallization rates in the DG and Hex phases were similar, while at high T_c (>35 °C) the PEO crystallization was slower in the DG phase than in the Hex phase. The Avrami exponent n-values for the DG and the Hex samples were similar (~ 1.8), yet the values of $\ln K$ in the DG phase were smaller than those in the Hex phase. This suggested that the linear growth rate was slower in the DG phase than in the Hex phase due to continuous curved channels in the DG phase.

Keywords: block copolymers; confined crystallization; crystallization kinetics

1. Introduction

Crystalline block copolymers are well-defined model systems showing complex hierarchical ordering and competition between crystallization and microphase separation on different length scales [1]. Recently, various issues related to polymer crystallization in microphase separated block copolymers have been investigated, such as confined versus unconfined (or breakout) crystallizations [2,3], crystal orientation in confined nanodomains [4–12] and 'templated' by oriented rubbery microphases [13,14], crystallization kinetics [2,10,15–19], and surface nanopatterning using crystalline block copolymers [20,21]. Different from crystalline homopolymers, the crystallization kinetics in crystalline block copolymers could be affected by multiple factors such as confined versus breakout and templated (weakly and/or partially confined) crystallizations [2,3], matrix hardness (or the glass transition temperature) [22], domain connectivity [16,23,24], morphology [3,15,19], and domain sizes [25,26]. In most cases, the crystallization kinetics is often complicated by more than one of the above factors simultaneously occurring in the system.

A polymer crystallization process consists of the primary nucleation and subsequent crystal growth (or secondary nucleation). The overall crystallization kinetics is determined by both nucleation rate and (linear) crystal growth rate. For confined crystallization, the interdomain connectivity through grain boundary, edge and screw dislocations

* Corresponding author. Tel. +1-860-486-8708; fax: +1-860-486-4745.
E-mail address: lei.zhu@uconn.edu (L. Zhu).

0032-3861/$ - see front matter © 2004 Published by Elsevier Ltd.
doi:10.1016/j.polymer.2004.02.068

plays an important role. It was found that when the microdomains were relatively isolated [the degree of isolation is the highest in the spherical phase, and decreases for the hexagonal cylinder (Hex) and lamellar (Lam) phases], homogeneous nucleation dictated the crystallization process and almost no crystal growth was needed to complete the crystallization [2,3,15,19,27,28]. The experimentally accessible T_cs were much lower than those in the unconfined crystallization. The Avrami exponent n was observed to be around one when a thermal nucleation was assumed, which was much smaller than that for homopolymers. This crystallization behavior was similar to the polymer crystallization in microdroplets (1–3 μm) [29], except for the much smaller domain sizes (10–30 nm) in block copolymers. All these results indicated the limited crystal growth in nanoconfined and isolated spaces. When the microdomains were continuous and inter-connected through grain boundary and dislocation such as in the Lam and Hex phases, heterogeneous nucleation usually dominated the crystallization process, and crystal growth in the continuous nano-geometries determined the crystal orientation [8,11]. For example, it was found that the crystal c-axes were parallel to the layer normal in the Lam phase [8], while they were perpendicular to the cylinder long axes in Hex phase [11], because the crystal growth direction usually conformed to the long direction of the microdomains. In these cases, the Avrami exponent n was observed to be higher than 1 (e.g., ~2) [22,30]. In certain examples, both homogeneous nucleation (at large undercoolings) and heterogeneous nucleation (at small undercoolings) were observed in the same sample [19,31]. For templated crystallization, although the lamellar crystals could not fully destroy the confinement, the inter-material dividing surfaces could be deformed by crystallization to facilitate nucleation and crystal growth. The crystallization kinetics was faster in these cases, and the Avrami exponent n was even higher (e.g., ~2–3) [2,3]. For breakout crystallizations, crystalline lamellae could completely break through the microdomain boundary and bridge neighboring domains together to form alternating crystalline-amorphous lamellar crystals. The Avrami exponent n equal to or higher than three was usually observed [2,3]. In most of these studies, samples with different molecular weights were used, since the emphasis was on the effect of microphase segregation strength on various modes of crystallization in crystalline block copolymers. However, it was difficult to directly compare the crystallization kinetics among different samples since they had different molecular weights.

One strategy to circumvent this difficulty is to blend amorphous homopolymers into the crystalline diblock copolymers (AB/A blends) to 'swell' only the amorphous microdomain. In this case, the morphology can be tuned from Lam to Hex and spheres, while the crystallizable blocks are the same. Recently, the effect of microdomain connectivity on the crystallization kinetics in nanoconfined layers was studied in PEO-*b*-polybutadiene (PEO-*b*-PB)/PB 'dry-brush' blends (the A homopolymer molecular weight is similar to that of the A blocks in the copolymer) [16]. The local lamellar feature of the PEO blocks was preserved, while the blends formed lamellar, cylindrical, and spherical vesicles with an increase in the PB content. The microdomain connectivity was largely depressed in spherical vesicles. It was observed that the crystallization kinetics of the PEO blocks in the interconnected lamellae was dominated by heterogeneous nucleation with the Avrami exponents n between 2 and 3, while it was first order ($n = 1$) kinetics in spherical vesicles and homogeneous nucleation started to become dominant with an increase in the homopolymer content.

It was found that the hardness and the glass transition temperature (T_g) of the amorphous blocks could substantially affect the crystallization kinetics of the crystallizable blocks in polystyrene-*b*-PEO/polystyrene (PS-*b*-PEO/PS) blends having a Hex morphology with the same volume fraction of PEO blocks [22]. The slow crystallization kinetics for the PEO blocks in a hard matrix was attributed to a much smaller Avrami exponent n than that in a rubbery matrix [22]. It was speculated that the mobility of the chains at the junction points between the two blocks could also affect the crystallization kinetics, although not much work has been carried out to confirm this hypothesis.

Different microdomain morphologies could also influence the crystallization kinetics, as in the 'wet-brush' AB/A blends (the A homopolymer molecular weight is smaller than that of the A block in the block copolymer) [3,15]. For example, when PB was blended into a lamellar PEO-*b*-PB diblock copolymer, the morphology changed from lamellae to cylinders, and finally to spheres with increasing the PB content. It was found that heterogeneous nucleation dominated the crystallization process in the Lam phase, while homogeneous nucleation became dominant in the Hex and spherical phases, regardless if the PB microdomains were crosslinked or not. The Avrami exponent n was ~2.5 for crystallization in the Lam phase, while it was 1.0 for crystallizations in the Hex and spherical phases. In AB/A 'wet-brush' polymer blends, the low molecular weight homopolymers more or less distribute uniformly in the A microdomain and thus the tethering (junction point) density decreases with increasing the homopolymer content. The change in the tethering density may also affect the crystallization kinetics of the crystallizable blocks.

In this study, we took a different approach to address the effect of confined geometry on block copolymer crystallization using the same material. A neat PS-*b*-PEO diblock copolymer, exhibiting multiple ordered mesophases, has been studied. In the quiescent melt, double gyroid (DG) was formed as the equilibrium phase morphology. Nevertheless, the DG phase transformed into a Hex phase as subjected to a large amplitude mechanical shear. Using a dilute solution crystallization approach, the Lam phase was obtained from single crystals. Differential scanning calorimetry (DSC) was used to study the crystallization kinetics in different

nanoconfined geometries. The major advantage in this study is to avoid the tethering density and microdomain connectivity changes such as in AB/A blends with different homopolymer contents.

2. Experimental

A PS-*b*-PEO diblock copolymer with $M_n^{PEO} = 11.6$ kg/mol and $M_n^{PS} = 18.5$ kg/mol was synthesized via sequential anionic block copolymerization of styrene and ethylene oxide, using a high vacuum technique [32]. The PEO volume fraction in the melt was 0.37, as determined by proton nuclear magnetic resonance (^{1}H NMR). The molecular weight distribution was determined by size exclusion chromatography (SEC) as 1.09. The sample was cast from a 5% (w/v) chloroform solution, and the solvent was allowed to evaporate at room temperature for 3 days, followed by drying in vacuum at 50 °C for 2 days. The dry samples were further annealed at 150 °C for 24 h to allow equilibrium microphase separation. The microphase-separated sample was subjected to a planar reciprocating shear at 120 °C under a dry nitrogen atmosphere, using a custom-built shear apparatus. The shear frequency was around 0.5 Hz, and the amplitude was ~150%. After shear, the sample was further annealed at 100 °C for 5 h to relax the residue stress.

Single crystal mats were obtained by growing PEO single crystals in a mixed dilute solution of chlorobenzene/octane = 1:1.1 (w/w). Self-seeding technique was used for solution crystallization: 5 mg block copolymer was first dissolved in 25 mL mixed solvent at 60 °C and subsequently crystallized at room temperature for 24 h. The solution containing white precipitates were slowly heated to 38.0 °C, the self-seeding temperature (T_s). Finally, the sample was isothermally crystallized at 25.0 °C for 24 h to ensure complete crystallization. Digi-sense temperature controller (Fisher Scientific Co.) was used to control the oil bath temperature within ± 0.1 °C. These single-crystal mats were washed twice by the mixed solvent before the solution was centrifuged at 12,000 rpm for 1 h. The sample was finally dried in vacuum at room temperature for 3 days. ^{1}H NMR and SEC experiments were performed on the single crystals. No significant changes in molecular weight and PEO composition were observed, suggesting there was no molecular fractionation due to the PEO-block crystallization in dilute solutions.

Two-dimensional (2D) small-angle X-ray scattering (SAXS) experiments were performed at the synchrotron X-ray beamline X3A2 in the National Synchrotron Light Source, Brookhaven National Laboratory. The wavelength of the X-ray beam was 0.154 nm. Silver behenate was used for calibration, which had a well-defined lamellar structure with the first order reflection at $q = 1.076\ \mathrm{nm}^{-1}$. Fuji imaging plates were used to record the SAXS patterns with a resolution of 100 μm. The typical data acquisition time was 1 min.

Transmission electron microscopy (TEM) experiments were performed on a Philips EM300 at an accelerating voltage of 80 kV. The samples for ultramicrotomy were embedded in standard epoxy which was cured at 50 °C for 24 h. Thin sections with ~75–100 nm thickness were obtained using a Leica Ultracut UCT microtome with a diamond knife at −40 °C. The thin sections were collected onto 400 mesh TEM grids, and were stained in RuO_4 vapor at room temperature for 20 min [33]. The flat single crystals were shadowed with Pt in vacuum at an angle of ca. 40°.

DSC experiments were carried out on a TA-2920 DSC to study the isothermal crystallization and subsequent melting behavior of the PEO blocks in the diblock copolymer. The T_g of the PS blocks was around 75 °C and the melting point of the PEO crystals was ~51 °C when the crystallization temperature (T_c) was lower than 40 °C. Less than 1 mg samples were used in the crystallization kinetics study to avoid possible thermal lag. Isothermal crystallization was conducted by quenching the samples (pre-melted at 70 °C for 2 min) to a preset T_c for measurements. The fully crystallized samples were then heated at a rate of 5–70 °C/min. The endothermic peak temperature was taken as the melting temperature (T_m). The weight percentage crystallinity was calculated using an equilibrium heat of fusion for perfect PEO crystals (8.66 kJ/mol) [34].

3. Results and discussion

3.1. Different phase morphologies in one PS-b-PEO diblock copolymer sample

The PS-*b*-PEO sample was cast from 5% (w/v) chloroform solution and annealed at 150 °C for 12 h to develop the ordered morphology. The sample was then heated above the order–disorder transition temperature (T_{ODT} ~210 °C) in a vacuum oven, and was quenched to 150 °C and held isothermally for 2 h. A pure DG phase was obtained, as confirmed by the one-dimensional (1D) SAXS results in Fig. 1A. The SAXS profile at 60 °C (in the melt) only shows two major reflections with the q-ratio being $\sqrt{6} : \sqrt{8}$, which are the DG (211) and (220) reflections. As the PEO blocks crystallize at 25 °C, multiple reflection peaks with the q-ratios being $\sqrt{6} : \sqrt{8} : \sqrt{14} : \sqrt{16} : \sqrt{20} : \ldots$ are observed, which are typical for the DG phase. The enhancement of the scattering intensity originates from the increase in the electron density difference after the PEO-block crystallization [30]. Comparing the SAXS curves at 60 °C and 25 °C, the DG (211) and (220) positions are exactly the same, indicating that confined PEO crystallization occurs in the DG phase. The d-spacing of the DG (211) planes is 20.0 nm. The a-axis of the double gyroid phase can thus be calculated to be 49.0 nm. The TEM micrographs of the DG phase [111]-projection are shown in Fig. 2A. Since the PEO

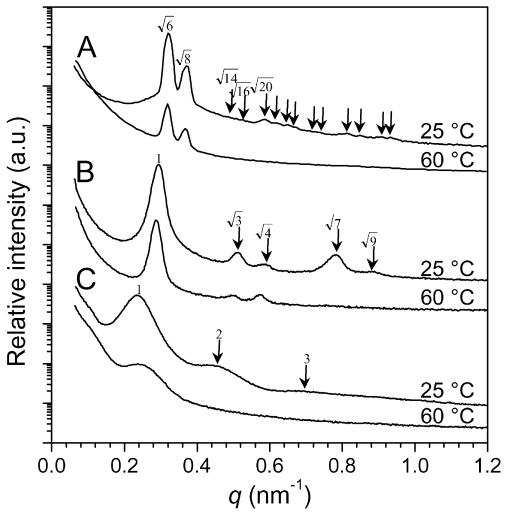

Fig. 1. One-dimensional (1D) SAXS profiles for (A) the DG, (B) the Hex, and (C) the Lam (single crystal mats) PS-*b*-PEO samples in both the crystalline (25 °C) and molten (60 °C) states.

microdomains are more readily stained by RuO_4, they appear darker than the PS microdomains in the micrographs. From this [111] projection image, the DG phase clearly shows the typical 'wagon wheel' morphology, and an enlarged area is shown as an inset. From the above SAXS results and the volume fraction of the PEO blocks, the average diameter of the DG channels can be estimated as ~9.4 nm.

After a large-amplitude reciprocating shear at 120 °C for 15 min, the DG phase transforms to a Hex phase. The 1D SAXS results for the Hex phase are shown in Fig. 1B. At 60 °C, multiple reflections are observed with a q-ratio of 1: $\sqrt{3}$: $\sqrt{4}$. After the PEO-block crystallization at 25 °C, up to five orders of reflections can be observed, and they have a q-relationship of 1: $\sqrt{3}$: $\sqrt{4}$: $\sqrt{7}$: $\sqrt{9}$. The first order diffraction is at $q = 0.298\ \text{nm}^{-1}$, and remains constant before and after the PEO-block crystallization. Again, this suggests that the confined crystallization occurs in the Hex phase. The distance between the neighboring cylinder centers is calculated to be 24.3 nm, and the diameter of the cylinder is 15.6 nm, as calculated from the volume fraction of PEO-blocks. We notice that the DG (211) reflection is close to that of the cylinder (100) reflection, which suggests the $[112]_{DG} \rightarrow [100]_{Hex}$ epitaxial relationship during the phase transformation between the DG and the Hex phases [35,36]. From the TEM observation in Fig. 2B, the cylinders appear to pack into an ordered hexagonal lattice and align their long axes perpendicular to the viewing plane. The inset of Fig. 2B shows the side-view of hexagonal cylinders running parallel to each other. Obviously, the PEO cylinders are perfectly aligned with grain sizes over 1 μm after the large-amplitude mechanical shear.

The lamellar geometry was successfully achieved by growing PEO single crystals in dilute solutions of chlorobenzene/octane mixture (1: 1.1 w/w). After single crystal formation, the PEO blocks crystallize into a single layer lamella, and the PS blocks are rejected to form

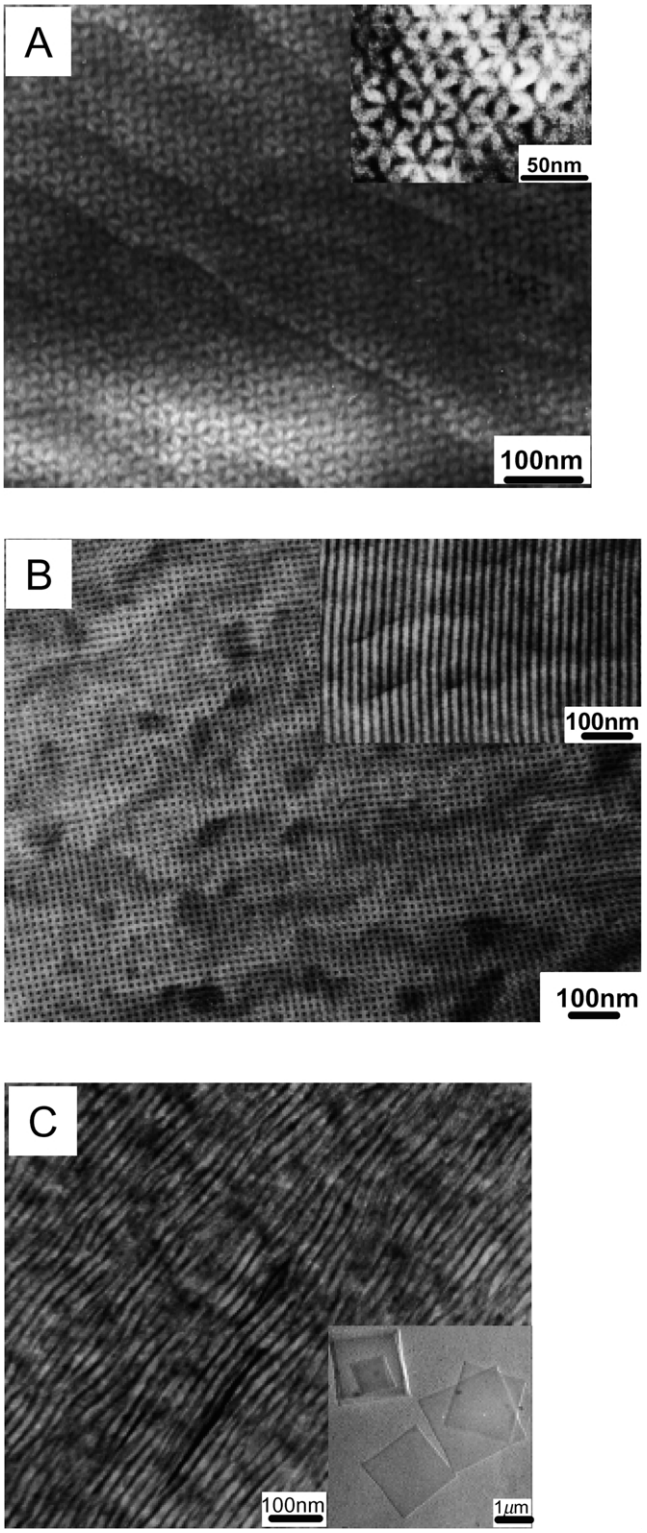

Fig. 2. Bright-field TEM micrographs of (A) the DG, (B) the Hex, and (C) the Lam (single crystal mats) PS-*b*-PEO samples. The inset in 2A is an enlarged area of the DG [111]-projection. The inset in 2B is the side-view of the Hex phase, and the inset in 2C is the flat-on view of PS-*b*-PEO single crystals. The single crystals were shadowed with Pt at an angle of ca. 40°.

protection layers at both the top and the bottom (see inset of Fig. 2C). The SAXS profiles of the single crystal mats are shown in Fig. 1C. Lamellar reflections can be clearly seen with q-ratios equal to 1: 2: 3. For these samples before (at 60 °C) and after (at 25 °C) PEO crystallization, the major SAXS reflection peaks do not change their positions, again indicating confined crystallization in the Lam phase. In the solid sample, the overall thickness is 26.5 nm, and the thickness of the PEO single crystals is 9.8 nm. The TEM micrograph of the single crystal mats cross-section is shown in Fig. 2C. Oriented lamellae can be clearly seen. The flat, square shaped PEO single crystals is shown as the inset in Fig. 2C. The average size of the single crystals is over 2 μm.

3.2. Nanoconfined crystallization in the DG, the Hex, and the Lam phases

Isothermal crystallizations at different T_cs were carried out for the DG, the Hex, and the Lam samples to compare the crystallization kinetics in different morphologies. Fig. 3A shows the DSC isothermal crystallization curves for the DG sample at different temperatures after pre-melting at 70 °C for 2 min. With increasing the T_c, the exothermic peak shifts to a longer crystallization time (t_c), and its intensity decreases continuously. The subsequent melting curves are shown in Fig. 3B, and a slightly increase in the T_m can be seen with increasing the T_c.

The isothermal crystallization kinetics for the PEO crystallization in the Hex phase is shown in Fig. 4A. Comparing with the isothermal crystallization curves in Fig. 3A, the exothermic peaks in Fig. 4A are less symmetric than those for the DG sample. The subsequent melting curves in Fig. 4B show broader melting peaks as compared with those for the DG sample in Fig. 3B.

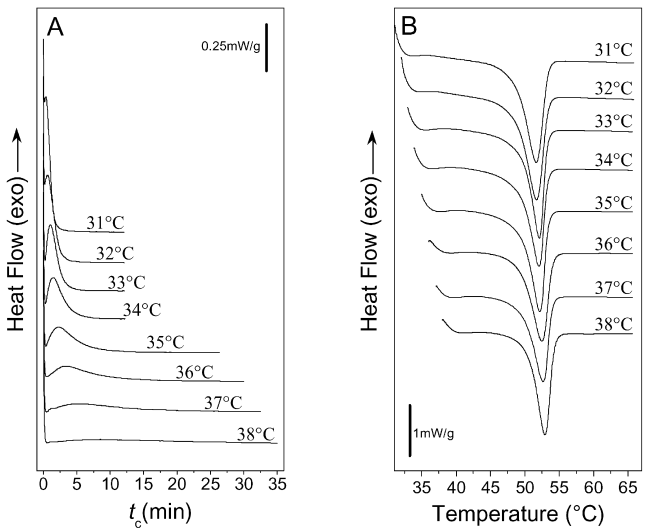

Fig. 3. (A) Isothermal crystallization curves for the DG sample at various T_cs. (B) The subsequent melting curves for the DG sample isothermally crystallized at different T_cs.

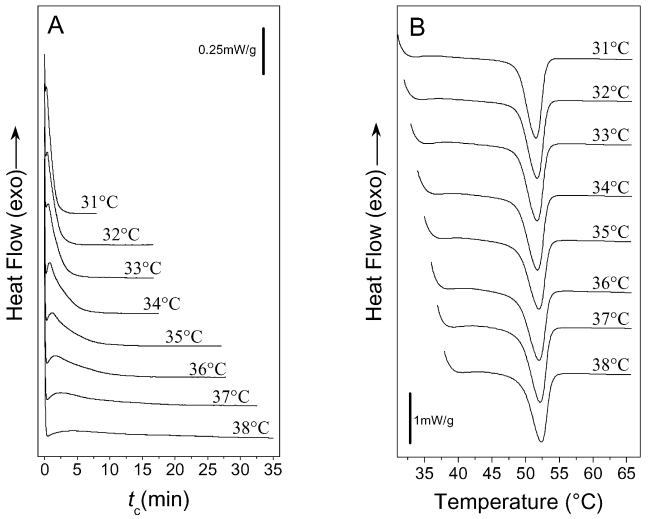

Fig. 4. (A) Isothermal crystallization curves for the Hex sample at various T_cs. (B) The subsequent melting curves for the Hex sample isothermally crystallized at different T_cs.

The isothermal crystallization kinetics for the Lam sample is shown in Fig. 5A, and the subsequent melting curves are in Fig. 5B. Comparing Fig. 5A with Figs. 3A and 4A, one can see faster kinetics in the Lam phase than in the DG and Hex phases. For example, the PEO blocks can crystallize reasonably fast even at temperatures higher than 40 °C. Compared with the DG and Hex samples, the T_m also shifts to higher values (53 ~ 55 °C). For all three samples (DG, Hex, and Lam), the crystallization of PEO block all occurs at relatively high T_cs (>30 °C), indicating a heterogeneous nucleation mechanism for PEO crystallization.

The Avrami plots can be obtained from the results in Figs. 3A, 4A, and 5A for the DG, Hex, and Lam samples. The early stage crystallizations can be fitted with the

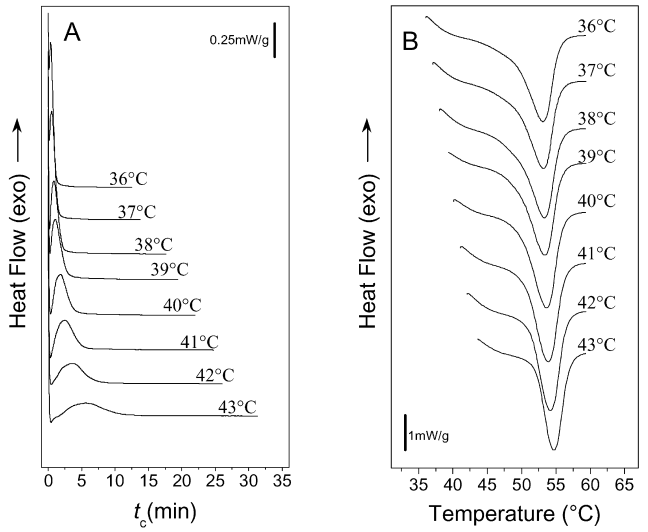

Fig. 5. (A) Isothermal crystallization curves for the Lam sample at various T_cs. (B) The subsequent melting curves for the Lam sample isothermally crystallized at different T_cs.

Avrami equation. The results are shown in Fig. 6A, B, and C, respectively. From these linear relationships, the Avrami parameters, the intercept [ln$K$] and the slope (n), can be obtained, as shown in Fig. 7. The Avrami exponent n represents the crystal growth dimension in confined spaces, and the results are shown in Fig. 7A. It is seen that the n values for the DG phase are almost constant around 1.8 for T_cs between 31 and 38 °C, while the Hex phase has slightly lower n values (~1.5–1.7) than the DG phase. These n values around 1.5 suggest approximately 1D crystal growth in the straight (Hex) and curved (DG) nano-channels. It is conceivable that since the DG phase has periodic nodes connecting 3-fold nano-channels together, the crystal growth inside the nodes could have higher crystal growth dimension than those in the channels. This would explain the slightly higher n values for the DG sample than for the Hex sample. The Avrami n values for the Lam phase are the highest, which remain constant around 2.25 for T_cs between 36 and 43 °C. The n values around 2.25 may suggest approximately 2D crystal growth inside nano-lamellar geometry.

The intercept, ln$K$, is related to nth power of the linear growth rate, geometric factor, and nucleation density (or rate). The results are shown in Fig. 7B. At relatively low T_cs, the ln$K$ values for the DG and Hex samples are the same. However, with increasing the T_c, the difference in the ln$K$ becomes more pronounced. Since the Avrami n values for the DG and Hex samples are similar (in a range of 1.5–2.0), the difference in the ln$K$ at the same temperature should directly relate to the difference in the linear growth rate and the nucleation density (or rate) in the nanoconfined spaces. In other words, the crystal linear growth rates and nucleation densities (or rates) are similar for the DG and Hex samples at low temperatures (e.g. 31 °C), while the linear growth rate is slower and the nucleation density (or rate) is lower in the DG sample than in the Hex sample at high temperatures (e.g. 38 °C).

These linear growth rate differences are further reflected in the overall crystallization rates, which is reciprocally proportional to the time required to reach certain crystallinity. Here, we denote the times, at which 10, 50, and 80 wt% crystallinities are reached, as $t_{10\%}$, $t_{50\%}$, and $t_{80\%}$, respectively, and they are plotted in Fig. 8. Below 35 °C, no obvious differences in $t_{10\%}$, $t_{50\%}$, and $t_{80\%}$ for the DG and Hex phases are observed. This is consistent with the above observations that at low T_cs there is not much difference in the ln$K$ between the DG and Hex samples. We speculate that at low temperatures, the nucleation density is relatively high. The crystal growth could be stopped more by the impingement with neighboring crystals than by the confined phase boundary (i.e. PS walls). In other words, at low temperatures the PEO crystals are too small to 'feel' the difference between curved (DG) and straight (Hex) nano-geometries, and thus the PEO crystal linear growth rate and overall nucleation density (or rate) are similar.

Above T_c = 35 °C, the differences in $t_{10\%}$, $t_{50\%}$, and $t_{80\%}$

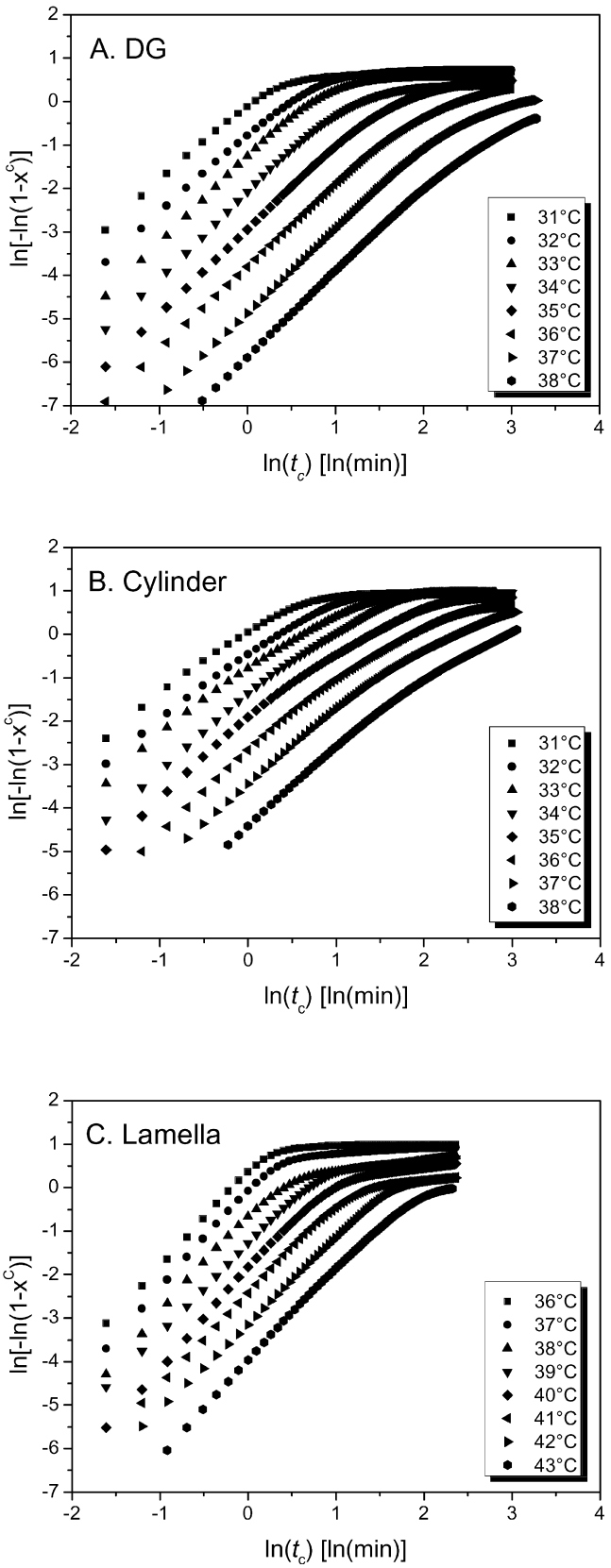

Fig. 6. Avrami plots for (A) the DG, (B) the Hex, and (C) the Lam samples at different T_cs.

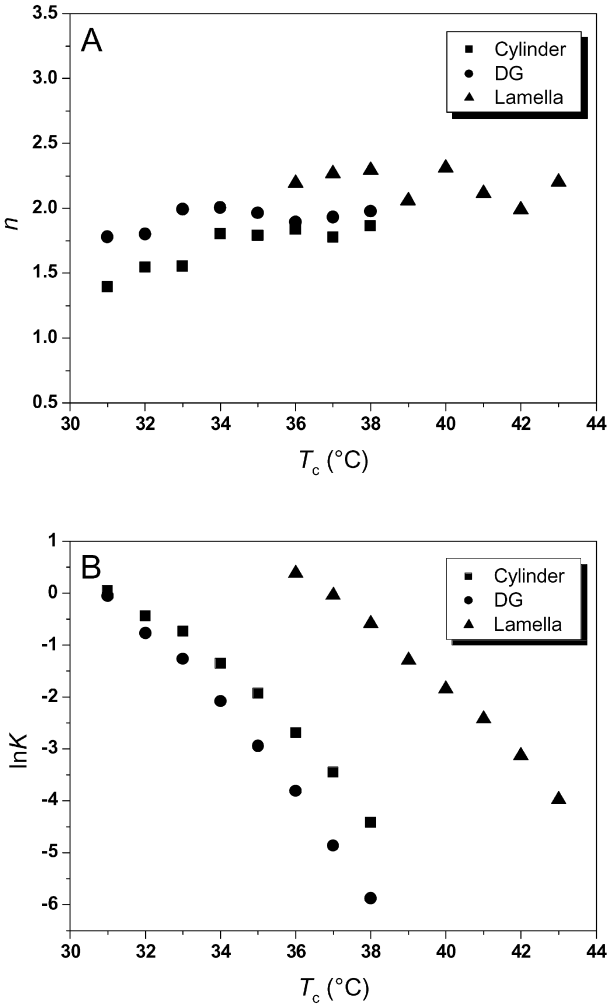

Fig. 7. Comparison of (A) Avrami intercepts ln$K$ and (B) exponents n for the DG, Hex, and Lam samples.

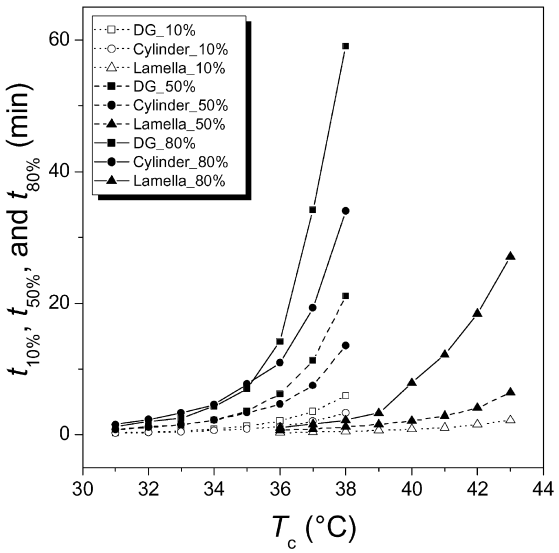

Fig. 8. Comparison of the overall crystallization times when the PEO crystallinity reaches 10 wt%, 50 wt%, and 80 wt% for the DG, Hex, and Lam samples.

gradually increases with T_c for the DG and Hex samples. However, the difference in the early crystallization stage ($t_{10\%}$) is much smaller than that in the late stages ($t_{50\%}$ and $t_{80\%}$). It is commonly considered that the primary nucleation process is dominant within 10 wt% crystallinity, and crystal growth becomes dominant after 10 wt% crystallinity. At high temperatures, the nucleation density dramatically drops for both the DG and Hex samples, and the distance between the neighboring nuclei could be quite far. During the crystal growth process, the chain-folded PEO ribbon crystals can grow to a longer distance in the Hex phase than in the DG phase, because the continuous curvature of the nano-channels in the DG phase forces the PEO crystal growth to break and/or branch from time to time. As a result, the crystal growth in the DG phase is more difficult and thus slower than in the Hex phase, especially at late crystallization stages and at high T_cs.

From Fig. 7B, the ln$K$ for the single crystal mats is much higher than both the DG and Hex samples at the same T_c. This clearly shows the morphological effects on the nano-confined crystallization between 1D and 2D confined geometries. From Fig. 7A, the n values of the Lam sample are slightly higher than those of the DG and the Hex samples (e.g., 2.2 versus 1.8). The large difference in the ln$K$ between the Lam and the DG/Hex samples should primarily originate from the differences in the linear growth rate and nucleation density (or rate) in different geometries. This is also consistent with the overall crystallization rate results in Fig. 8. The $t_{10\%}$, $t_{50\%}$, and $t_{80\%}$ for the Lam sample are substantially smaller than those for the DG and Hex samples at the same T_c, which suggests that both nucleation density (or rate) and linear crystal growth rate are higher in the 1D confined lamellar geometry than in the 2D confined DG/Hex geometries.

The crystallinity comparison for the DG, Hex, and Lam samples is shown in Fig. 9. The DG sample has the lowest

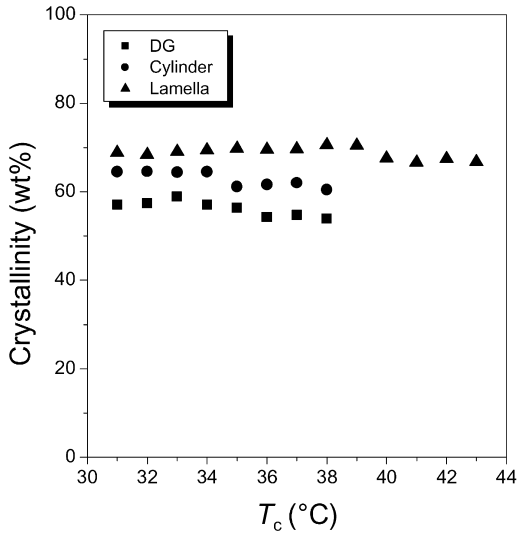

Fig. 9. The PEO crystallinity comparison for the DG, Hex, and Lam samples.

crystallinity (~57 wt%) at the same T_c, since the continuous curvature in the DG phase introduces more defects in the PEO crystals and thus less packing density. The Lam sample has the highest crystallinity (~70 wt%) at the same T_c, since the PEO lamellar crystals in the lamellar geometry have fewer defects and thus higher packing density than those in both the DG and the Hex samples.

The melting points for the DG, the Hex, and the Lam samples are given in Fig. 10. It is seen that the T_ms slightly increase with T_c for all three samples. The DG and the Hex samples have very similar T_m, while the T_m for the Lam sample is higher. Again, this may reflect the morphological effects on the thermodynamic stability of PEO crystals. In the Lam samples, the PEO crystals have higher stability than in the DG/Hex samples.

4. Conclusions

Multiple phase morphologies such as the DG, Hex, and Lam have been obtained in one PS-*b*-PEO diblock copolymer having a volume fraction of PEO ~37 vol%. After solution casting and high temperature annealing, a DG phase was obtained. However, it transformed into a Hex phase upon a large-amplitude mechanical shear. Solution crystallization of the PS-*b*-PEO diblock copolymer generated lamellar single crystals with the crystalline PEO layer sandwiched between the PS layers. Since the T_g of the PS blocks was higher than the T_m of PEO crystals, nanoconfined crystallization was ensured in different phases. The confined crystallization was also verified by SAXS and TEM measurements. Using DSC, morphological effects on nanoconfined crystallization kinetics were compared among the DG, the Hex, and the Lam phases. The crystallization kinetics was faster in 1D-confined Lam phase than in the DG and the Hex phases. Also, the PEO crystals possessed higher crystallinity and thermodynamic stability in the Lam phase than in the DG and the Hex phases. For 2D-confined crystallization in the DG and the Hex phases, there was no obvious difference in the crystallization kinetics at low T_cs, due to the relatively high nucleation density and the small crystal sizes. It was conceivable that these small PEO crystals didn't 'feel' the morphological difference between the curved and straight channels in the DG and the Hex samples before the rapid impingement of neighboring crystals. At high T_cs, the crystal growth rate and nucleation density (or rate) in the DG phase drastically decreased compared to those in the Hex phase. This can be attributed to the morphological difference between the DG and the Hex phases. Since the DG phase contained continuously curved channels, it might be difficult for the PEO crystals to grow inside.

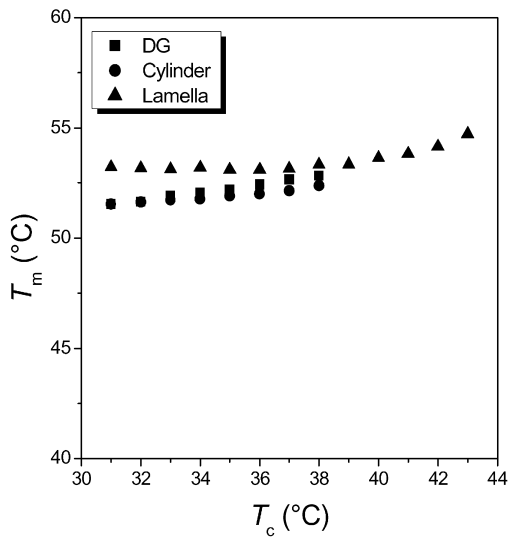

Fig. 10. The T_m comparison for the DG, Hex, and Lam samples.

Acknowledgements

LZ is grateful to the startup funds provided by the University of Connecticut. This work was supported by the University of Connecticut Research Foundation and partially by the National Science Foundation (NSF) CAREER award (DMR-0348724). SZDC acknowledges the support of NSF (DMR-0203994). The synchrotron SAXS experiments were carried out in the National Synchrotron Light Source, Brookhaven National Laboratory, which is supported by the Department of Energy (DOE).

References

[1] Muthukumar M, Ober CK, Thomas EL. Science 1997;277:1225.
[2] Loo Y-L, Register RA, Ryan AJ. Macromolecules 2002;35:2365.
[3] Xu J-T, Fairclough JPA, Mai S-M, Ryan AJ. Macromolecules 2002; 35:6937.
[4] Hamley IW, Fairclough JPA, Terrill NJ, Ryan AJ, Lipic PM, Bates FS, Towns-Andrews E. Macromolecules 1996;29:8835.
[5] Hillmyer MA, Bates FS. Macromol Symp 1997;117:121.
[6] Quiram DJ, Register RA, Marchand GR. Macromolecules 1997;30: 4551.
[7] Quiram DJ, Register RA, Marchand GR, Adamson DH. Macromolecules 1998;31:4891.
[8] Zhu L, Cheng SZD, Calhoun BH, Ge Q, Quirk RP, Thomas EL, Hsiao BS, Yeh F, Lotz B. J Am Chem Soc 2000;122:5957.
[9] Park C, De Rosa C, Fetters LJ, Thomas EL. Macromolecules 2000;33: 7931.
[10] Loo YL, Register RA, Adamson DH. Macromolecules 2000;33:8361.
[11] Huang P, Zhu L, Calhoun BH, Ge Q, Quirk RP, Cheng SZD, Thomas EL, Hsiao BS, Yeh F, Liu L, Lotz B. Macromolecules 2001;34:6649.
[12] Zhu L, Huang P, Chen WY, Ge Q, Quirk RP, Cheng SZD, Thomas EL, Lotz B, Hsiao BS, Yeh F, Liu L. Macromolecules 2002;35:3553.
[13] Hamley IW, Castelletto V, Floudas G, Schipper F. Macromolecules 2002;35:8839.
[14] Fairclough JPA, Mai S-M, Matsen MW, Bras W, Messe L, Turner SC, Gleeson AJ, Booth C, Hamley IW, Ryan AJ. J Chem Phys 2001;114: 22.
[15] Chen H-L, Wu J-C, Lin T-L, Lin JS. Macromolecules 2001;34:6936.

[16] Chen H-L, Lin S-Y, Huang Y-Y, Chiu F-C, Liou W, Lin JS. Macromolecules 2002;35:9434.
[17] Chen H-L, Wu J-C, Lin T-L, Lin JS. J Polym Sci, Polym Phys Ed 2002;40:519.
[18] Loo YL, Register RA, Ryan AJ. Phys Rev Lett 2000;84:4120.
[19] Loo Y-L, Register RA, Ryan AJ, Dee GT. Macromolecules 2001;34: 8968.
[20] Reiter G, Castelein G, Hoerner P, Riess G, Blumen A, Sommer J. Phys Rev Lett 1999;83:3844.
[21] De Rosa C, Park C, Thomas EL, Lotz B. Nature 2000;405:433.
[22] Zhu L, Mimnaugh B, Ge Q, Quirk RP, Cheng SZD, Thomas EL, Lotz B, Hsiao BS, Yeh F, Liu L. Polymer 2001;42:9121.
[23] Hong S, MacKnight WJ, Russell TP, Gido SP. Macromolecules 2001; 34:2876.
[24] Hong S, Yang LZ, MacKnight WJ, Gido SP. Macromolecules 2001; 34:7009.
[25] Huang P, Zhu L, Guo Y, Ge Q, Jing AJ, Chen WY, Quirk RP, Cheng SZD, Thomas EL, Lotz B, Hsiao BS, Avila-Orta CA, Sics I. Macromolecules 2004; Submitted for publication.
[26] Massa MV, Dalnoki-Veress K. Eur Phys J Ed 2003;11:191.
[27] Röttele A, Thurn-Albrecht T, Sommer J-U, Reiter G. Macromolecules 2003;36:1257.
[28] Reiter G, Castelein G, Sommer J-U, Röttele A, Thurn-Albrecht T. Phys Rev Lett 2001;87:5918.
[29] Koutsky JA, Walton AG, Baer EJ. Appl Phys 1967;38:1832.
[30] Zhu L, Cheng SZD, Calhoun BH, Ge Q, Quirk RP, Thomas EL, Hsiao BS, Yeh F, Lotz B. Polymer 2001;42:5829.
[31] Lotz B, Kovacs AJ. Polym Prepr (Am Chem Soc, Div Polym Chem) 1969;10(2):820.
[32] Morton M, Fetters LJ. Rubber Chem Technol 1975;48:359.
[33] Trent JS, Scheinbeim JI, Couchman PR. Macromolecules 1983;16: 589.
[34] Wunderlich B. Thermal analysis. Boston: Academic Press; 1990.
[35] Schulz MF, Bates FS, Almdal K, Mortensen K. Phys Rev Lett 1994; 73:86.
[36] Matsen MW. Phys Rev Lett 1998;80:4470.